Monthly Notices
of the
ROYAL ASTRONOMICAL SOCIETY

MNRAS **498,** 4562–4576 (2020)
Advance Access publication 2020 September 2

doi:10.1093/mnras/staa2654

Active galactic nucleus and dwarf galaxy gas kinematics

Christina M. Manzano-King ★ and Gabriela Canalizo
University of California, Department of Physics and Astronomy, Riverside, CA, 92521 USA

Accepted 2020 August 25. Received 2020 August 23; in original form 2020 July 24

ABSTRACT

We present spatially resolved kinematic measurements of stellar and ionized gas components of dwarf galaxies in the stellar mass range $10^{8.5}$–10^{10} $M_{\odot}$, selected from Sloan Digital Sky Survey DR7 and DR8 and followed up with Keck/Low-Resolution Imaging Spectrometer spectroscopy. We study the potential effects of active galactic nuclei (AGNs) on Galaxy-wide gas kinematics by comparing rotation curves of 26 Galaxies containing AGNs, and 19 control Galaxies with no optical or infrared signs of AGNs. We find a strong association between AGN activity and disturbed gas kinematics in the host Galaxies. While star-forming Galaxies in this sample tend to have orderly gas discs that co-rotate with the stars, 73 per cent of the AGNs have disturbed gas. We find that 5 out of 45 Galaxies have gaseous components in counter-rotation with their stars, and all Galaxies exhibiting counter-rotation contain AGNs. Six out of seven isolated Galaxies with disturbed ionized gas host AGNs. At least three AGNs fall clearly below the stellar–halo mass relation, which could be interpreted as evidence for ongoing star formation suppression. Taken together, these results provide new evidence supporting the ability of AGN to influence gas kinematics and suppress star formation in dwarf galaxies. This further demonstrates the importance of including AGN as a feedback mechanism in galaxy formation models in the low-mass regime.

Key words: galaxies: active – galaxies: dwarf – galaxies: evolution – galaxies: kinematics and dynamics.

1 INTRODUCTION

In the Lambda cold dark matter (ΛCDM) model of structure formation, dark matter haloes form from the gravitational collapse of primordial density fluctuations. Within these haloes, baryons collapse into a rotating disc with the same angular momentum as the dark matter halo. With sufficient radiative cooling, the gas is able to collapse and form stars, resulting in a co-rotating disc of gas and stars within a dark matter halo with a density profile that can be approximated by a simple formula known as the Navarro-Frenk-White (NFW) profile (Navarro, Frenk & White 1997). On large scales, the ΛCDM model of structure formation agrees well with observations of massive galaxies and clusters.

However, large discrepancies in the low-mass regime raise doubts about ΛCDM. For example, there is a large disagreement between the number of small dark matter haloes and observed dwarfs (missing satellite problem; Klypin et al. 1999; Moore et al. 1999). There is also a conspicuous absence of observed large satellites compared to predictions (too-big-to-fail problem; Read et al. 2006; Boylan-Kolchin, Bullock & Kaplinghat 2011). Finally, rotation profiles of dwarfs show a variety of inner slopes, indicating a diversity of dark matter halo profiles, many of which are in disagreement with the predicted NFW dark matter density profile (cusp versus core problem; Flores & Primack 1994; Simon et al. 2005; Oh et al. 2011). These departures from the ΛCDM model have prompted some to look into warm (e.g. Lovell et al. 2014) or self-interacting dark matter (e.g. Rocha et al. 2013). A promising alternative to rethinking the nature of dark matter is to investigate the effects of baryonic feedback on star formation.

High-resolution simulations conclude that baryonic processes can be used to reconcile the observed properties of dwarf galaxies with ΛCDM (Wetzel et al. 2016). Theoretical work commonly attributes star formation suppression in dwarf galaxies to heating from the UV background during reionization (e.g. Katz et al. 2020), stellar radiation (e.g. Emerick, Bryan & Mac Low 2018), and supernova feedback (e.g. Hu 2019). Indeed, powerful star formation-driven outflows are observed in starbursting dwarf galaxies (Martin 1998; Strickland & Stevens 2000), and some observational evidence suggests that stellar feedback may dominate in dwarf galaxies (Martín-Navarro & Mezcua 2018).

Stellar feedback is only part of the picture, as the role of active galactic nucleus (AGN) feedback in dwarfs becomes harder to ignore. Evidence of AGN via optical and infrared (IR) indicators has been detected in hundreds of nearby dwarf galaxies (Reines, Greene & Geha 2013; Moran et al. 2014; Sartori et al. 2015; Baldassare, Geha & Greene 2020; Birchall, Watson & Aird 2020). Kaviraj, Martin & Silk (2019) report the IR-selected AGN occupation fraction in high-mass galaxies to be 1–3 per cent, while the same criteria yield a 10–30 per cent fraction in dwarf galaxies ($M_* \sim 10^{8-10}$ $M_{\odot}$). Given that there are several factors that hinder the detection of AGN in dwarfs (Satyapal, Abel & Secrest 2018; Cann et al. 2019), this large AGN fraction can be regarded as a lower limit. These studies suggest that AGNs are common and potentially important phenomena in the low-mass regime.

Additionally, observational evidence of AGN-driven outflows in dwarf galaxies has begun to surface (Bradford et al. 2018; Penny et al. 2018; Dickey et al. 2019; Manzano-King, Canalizo & Sales 2019). Each of these studies presents observations of AGN

★ E-mail: cking012@ucr.edu

coexisting with kinematically disturbed gas. Such disturbances are distinguished by broadened components in their emission line profiles and velocity measurements indicating gas that is disconnected or even counter-rotating with respect to their stars. For example, Starkenburg et al. (2019) (henceforth, S19) use data from Illustris (Genel et al. 2014; Vogelsberger et al. 2014) to investigate the origin of star–gas counter-rotation in dwarf galaxies. By examining the evolutionary history of simulated galaxies with counter-rotating gas, they found that such counter-rotating components require removal of the original gas reservoir and re-accretion of new gas, with misaligned angular momentum. S19 identify two plausible mechanisms for gas removal: stripping from an encounter with a neighbouring galaxy or AGN outflow events.

The role of AGN feedback in galaxy formation and evolution is not well understood in general. The shallow potential wells of dwarf galaxies leave them particularly susceptible to feedback, making them ideal laboratories to study how the energy output of an AGN couples to the gas in the host galaxy. The discovery of AGN-driven outflows in the dwarf regime challenges current conceptions of feedback in dwarf galaxies and raises the question of whether the gas in these outflows permanently escapes the halo. In this paper, we explore the connection between AGN and kinematically disturbed gas and present further evidence of AGN feedback in dwarf galaxies.

Throughout the paper, we assume the cosmological model $H_0 = 71\,\mathrm{km\,s^{-1}\,Mpc^{-1}}$, $\Omega_\mathrm{m} = 0.27$, and $\Omega_\Lambda = 0.73$.

2 DATA

Our complete sample contains 50 nearby ($z = 0.05$) dwarf Galaxies (roughly $M_\star < 10^{10}\,\mathrm{M}_\odot$) drawn from the Sloan Digital Sky Survey (SDSS) (Blanton et al. 2017). SDSS is 95 per cent complete to r-band magnitude of 22.2, which is well below the magnitude range covered in this sample ($r \approx 12$–17). 29 of the Galaxies in our sample are classified as AGN based on emission line flux ratios that fall above the Kauffmann et al. (2003) star-forming sequence on the Baldwin, Phillips, and Terlevich (BPT) diagnostic (Baldwin, Phillips & Terlevich 1981) or the presence of detectable He II emission (Shirazi & Brinchmann 2012). This sample of 29 dwarf Galaxies hosting AGN was selected from the parent samples of Reines et al. (2013), Moran et al. (2014), Sartori et al. (2015), and Oh et al. (2015) based on right ascensions that could be observed during our allotted Keck time. In order to facilitate spatially resolved kinematic measurements, we prioritized spatially extended galaxies and excluded face-on galaxies whenever possible.

To enable comparison between galaxies with and without AGNs, we selected a control sample of 21 star-forming Galaxies from SDSS Data Release 8, based on the absence of optical and IR signatures of AGN. The control sample was selected by applying the same stellar mass and redshift cuts used to build the AGN sample, and then excluding objects with emission line flux ratios falling above the star-forming sequence on the BPT diagram. We also excluded all potential AGNs using the *WISE* mid-IR colour criteria (Jarrett et al. 2011; Stern et al. 2012) and further excluded all galaxies with detectable He II emission. The BPT diagnostic diagram and distributions of the redshifts and stellar masses of our full sample are shown in Fig. 1.

We collected long-slit spectroscopy of 50 Galaxies using the Low-Resolution Imaging Spectrometer on the Keck I telescope (LRIS; Oke et al. 1995; C. Rockosi et al. 2010). Observation dates, conditions, and spectrograph set-ups for each object are listed in Table 1. The DIMM seeing (full width at half-maximum value of a star observed at zenith, at 5000 Å) is listed for each night. The slit position angles (PAs) were determined by fitting r-band SDSS

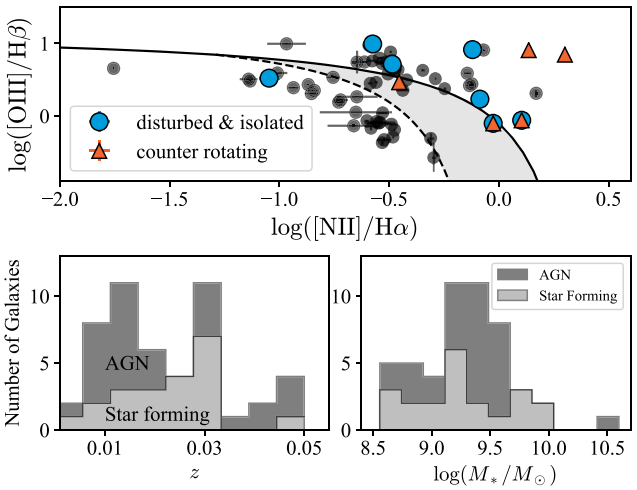

Figure 1. Top: BPT diagnostic for all 50 Galaxies in this sample. The dotted line denotes the Kauffmann et al. (2003) classification cut-off, and the solid line is the Kewley et al. (2001) maximum starburst line. Blue circles indicate isolated Galaxies with disturbed gas and with no neighbours of comparable mass (i.e. the neighbouring galaxy is at least 0.75 times the stellar mass of the dwarf) within 1.5 Mpc (see Section 4.4). Galaxies with counter-rotating stellar and gas components are marked as orange triangles. Bottom: Stacked histograms of redshift and stellar mass of the Galaxies presented in this paper. Dark grey represents AGN hosts and light grey represents star-forming Galaxies.

photometry using the IRAF ellipse task. By placing the slit along the semimajor axes determined by these ellipse fits, as shown in Fig. 2, we obtained spatially resolved spectra, presumably perpendicular to the rotation axis of each Galaxy.

The LRIS data were reduced using a PYTHON pipeline to automate the standard IRAF reduction tasks. Flexure on the red camera was corrected using the average shift in sky lines. Sky lines are sparse in the wavelength range covered by the blue CCD, so each Galaxy spectrum on the blue side was redshift corrected using the redshift measured from the flexure-corrected red spectrum. Flexure on the blue CCD was then calculated by comparing redshift-corrected Galaxy emission lines with their expected rest-frame values. The long-slit spectra were rectified along both the wavelength and spatial axes, yielding two-dimensional spectra where each pixel row along the spatial axis is a fully reduced one-dimensional spectrum.

3 ANALYSIS

3.1 Spatially resolved spectra

The long-slit spectra have been rectified along both the wavelength and spatial axes, creating a 2D spectrum where each pixel row is a fully reduced 1D spectrum. Much of our analysis depends on fitting subtle spectral features, and thus requires high signal to noise (S/N), especially in the dim outskirts of each Galaxy. To achieve the required S/N, we spatially bin the spectra, using larger bins on the outskirts of the Galaxy, as shown in Fig. 3.

Spectra were extracted along the slit by summing pixel rows until the target S/N ratio (typically 15–20) or maximum bin size was reached. In order to prevent summing the entire image and losing spatial data, the maximum bin size is set to be 20 per cent of the spatial axis. The S/N was measured using the mean and standard deviation of a relatively featureless portion of the stellar spectrum,

Table 1. LRIS configuration for each object, using the 1 arcsec slit placed along the semimajor axis of each Galaxy. For the blue side (LRIS-B), we used the 600 groove mm^{-1} grism blazed at 4000 Å, yielding a dispersion of 0.63 Å $pixel^{-1}$. We used three set-ups on the red side (LRIS-R): A: 600 groove mm^{-1} grating blazed at 5000 Å, 5600 Å dichroic, yielding a dispersion of 0.80 Å $pixel^{-1}$; B: 900 groove mm^{-1} grating blazed at 5500 Å, 5600 Å dichroic, yielding a dispersion of 0.53 Å $pixel^{-1}$; and C: 1200 groove mm^{-1} grating blazed at 7500 Å, 5000 Å dichroic, yielding a dispersion of 0.40 Å $pixel^{-1}$. Objects with superscript a denote Galaxies excluded from this analysis based on the limited spatial extent of their stellar velocity curves.

Name in SDSS	Observation date	Seeing (arcsec)	Slit PA CCW N	Red set-up	Exposure time (s)
J002145.80+003327.3	2015-12-05	0.59	42.4	B	1200
J004214.99−104415.0	2015-12-04	0.55	26.9	B	1200
J010005.94−011059.0	2015-12-04	0.55	51.2	B	1200
J015645.30−003737.8	2015-12-04	0.55	126	B	1200
J024656.39−003304.8[a]	2015-12-04	0.55	131.9	B	1200
J030040.20+000113.3	2015-12-04	0.55	28.3	B	2400
NGC 1569[a]	2015-12-04	0.55	122.5	B	2400
J075538.19+240103.5	2015-12-04	0.55	0	B	2400
J080212.06+103234.1	2015-12-05	0.59	100.7	B	2400
J080228.83+203050.2	2015-12-04	0.55	73.3	B	2400
J081145.29+232825.7	2015-12-04	0.55	0	B	2400
J081256.37+545808.4	2015-12-05	0.59	32.77	B	1200
J084025.54+181858.9	2015-12-04	0.55	101	B	2400
J084234.51+031930.7	2015-12-05	0.59	0	B	1200
J085125.81+393541.7	2015-03-24	0.70	−43.96	C	1200
J090613.75+561015.5	2015-12-04	0.55	0	B	2400
J091122.24+615245.2	2015-03-24	0.70	−13	C	2400
J092149.44+233438.7	2015-12-05	0.59	156.3	B	1200
J093251.11+314145.0	2015-03-25	0.58	−94.6	B	1200
J094800.79+095815.4	2015-12-05	0.59	117.8	B	1200
J094941.20+321315.9	2015-12-04	0.55	64	B	1200
J095418.16+471725.1	2015-12-05	0.59	0	B	2400
J100200.96+591508.3	2015-12-04	0.55	148.5	B	1200
J100551.19+125740.6	2015-12-04	0.55	60.1	B	1200
J100935.66+265648.9	2015-12-05	0.59	45.5	B	1200
J101440.21+192448.9	2015-03-25	0.58	−57.58	B	1200
J114343.76+550019.2	2015-03-25	0.58	−117.58	B	1200
J122342.82+581446.2[a]	2015-03-24	0.70	−106.86	C	1200
J130434.92+075505.0	2017-06-25	0.85	0.0	B	1200
J130724.63+523715.2	2015-03-25	0.58	74.09	B	2400
J131503.77+223522.7[a]	2015-03-24	0.70	−144.8	C	1200
J134332.09+253157.7	2015-03-24	0.70	−21.33	C	2400
J140116.03+542507.4	2015-03-25	0.58	81.76	B	1200
J140228.72+091856.4	2017-06-24	1.17	120	B	1200
J140510.39+114616.9	2017-06-25	0.85	12	A	1200
J140735.47+503242.7	2017-06-25	0.85	163	A	2400
J141208.47+102953.8	2017-06-24	1.17	0.0	B	1200
J144252.78+205451.6	2017-06-24	1.17	101	B	1200
J145843.39+113745.4	2017-06-25	0.85	19	A	1200
J151116.53+233421.6	2017-06-25	0.85	165	A	1200
J154603.78+031339.4	2017-06-24	1.17	31	B	1200
J160839.57+120038.5	2017-06-25	0.85	174	A	1200
J162307.88+391847.5	2017-06-24	1.17	80	B	1200
J162335.06+454443.6	2017-06-25	0.85	40	A	1200
J164428.48+435904.2	2017-06-24	1.17	82	B	1200
J170639.14+334103.4	2017-06-25	0.85	156	A	1200
J171759.66+332003.8	2017-06-24	1.17	68	B	1200
J172125.92+281134.9	2017-06-24	1.17	168	B	1200
J172208.82+280155.8	2017-06-24	1.17	130	B	1200
J232028.21+150420.9[a]	2015-12-04	0.55	122.2	B	1200

just redward of [O III]λ5007. The next bin would begin at the central pixel of the last bin. Fig. 3 shows the S/N of each pixel row along the spatial axis (black). Vertical grey lines mark the divisions between bins, and the green line indicates the S/N when all pixel rows within each bin is summed.

3.2 Emission line fluxes

In order to measure accurate emission line fluxes, it is necessary to account for stellar absorption, which primarily affects the Balmer emission lines. The Penalized Pixel-Fitting software (PPXF; Cappellari 2017) is used to fit and subtract the stellar continuum following

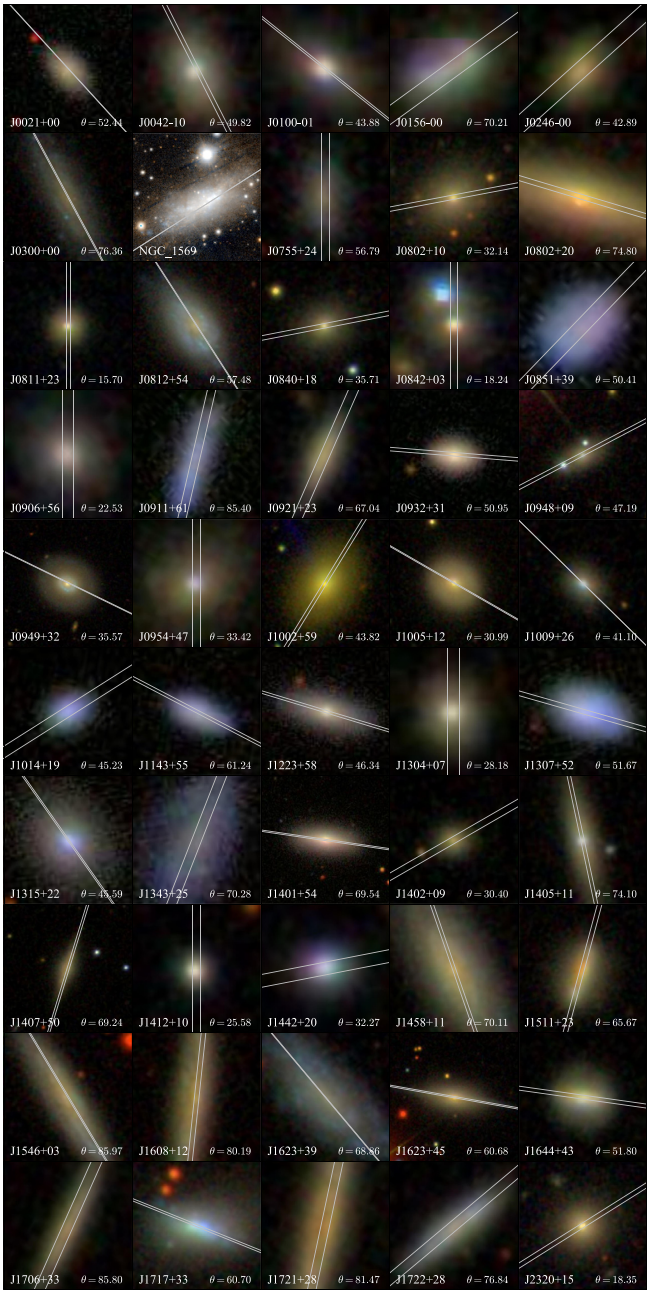

Figure 2. Colour images of all 50 dwarf Galaxies in our sample. All images were generated using the SDSS DR12 finding chart tool, with the exception of NGC 1569, which is outside of the SDSS footprint. The NGC 1569 thumbnail (second row, second column) is a PanSTARS z- and g-band colour image rendered in the Aladin Lite Viewer with a 3 arcmin field of view (∼1 kpc on a side). Each SDSS image is scaled to 10 kpc on a side and the placement of the 1 arcsec-wide slit is shown in light grey.

the method described in Manzano-King et al. (2019) (henceforth, Paper I), Section 3.1.

After subtracting the best-fitting stellar population model of the Galaxy, the residual emission lines were fitted using a custom Bayesian Markov chain Monte Carlo maximum likelihood sampling algorithm, implemented using the PYTHON package *EMCEE* (Foreman-Mackey et al. 2013). A single-Gaussian model was used to fit emission lines for each Galaxy in this sample, except in 13 cases when a second Gaussian component was needed (Paper I). In these

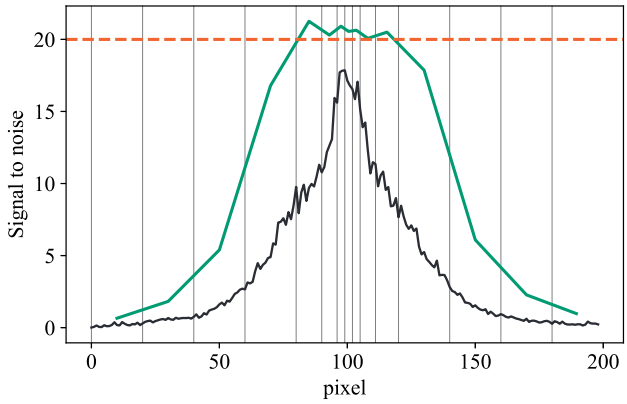

Figure 3. Pixel number along the spatial axis is shown on the x-axis. The y-axis shows the signal-to-noise ratio of a featureless portion of the spectrum redward of [O III]λ5007. Moving along the slit, we summed pixel rows (black) until the integrated spectrum's signal-to-noise ratio (green) reached the target S/N (red) or the maximum bin size was reached. The minimum bin size is 3 pixel rows, which sometimes results in even higher S/N. Exposure times for each object were chosen with the intention of obtaining sufficient S/N in the outskirts, so the bin size is dependent on the observational set-up used.

13 cases, the BPT flux ratios of the narrow component of the emission lines are shown in Fig. 1 and used when classifying these Galaxies as AGN or star forming.

3.3 Multicomponent velocity measurements

In the PPXF software, emission lines are modelled as Gaussians and fitted simultaneously with stellar templates. Each stellar and gas template can be matched to a unique kinematic component, enabling the decomposition of multiple distinct line-of-sight velocities for stars and various species of emission lines. Each spatially resolved velocity measurement presented in this work consists of three components: stellar, ionized hydrogen, and forbidden gas emission.

To avoid systematic errors introduced by wavelength calibration on the blue CCD, we fit ∼1000 Å sections of the spectrum using PPXF. Due to the strength of the H β and [O III] emission lines, and their proximity to the stellar feature Mg Ib, we measured line-of-sight velocities using the spectral region at a rest wavelength of 4500–5560 Å whenever favourable. Five Galaxies were observed using the 5000 Å dichroic, which disrupts the H β, [O III] region of the spectrum. In these cases, stellar and gas kinematics were measured by fitting the portion of the spectrum containing [O II] and Balmer break (3650–4550 Å). In cases where the [O III] lines were faint, the fitting area containing H α, [N II], and [S II] (6400–6800 Å) enabled gas velocity measurements to extend to a larger radius than fitting the 4500–5560 Å region. An example of fits to these three regions is shown in Fig. 4.

13 Galaxies in our sample have gas profiles that cannot be accurately modelled by a single Gaussian. In these cases, two Gaussian components were used for each emission line: a narrow and a broad. The velocity measurements presented in this work were obtained from the narrow Gaussian components.

3.4 Circular velocity curves

We extracted spatially resolved spectra along the semimajor axis of each Galaxy by summing pixel rows, as described in Section 3.1. Multicomponent line-of-sight velocity measurements were then taken from each spectrum following the method outlined in

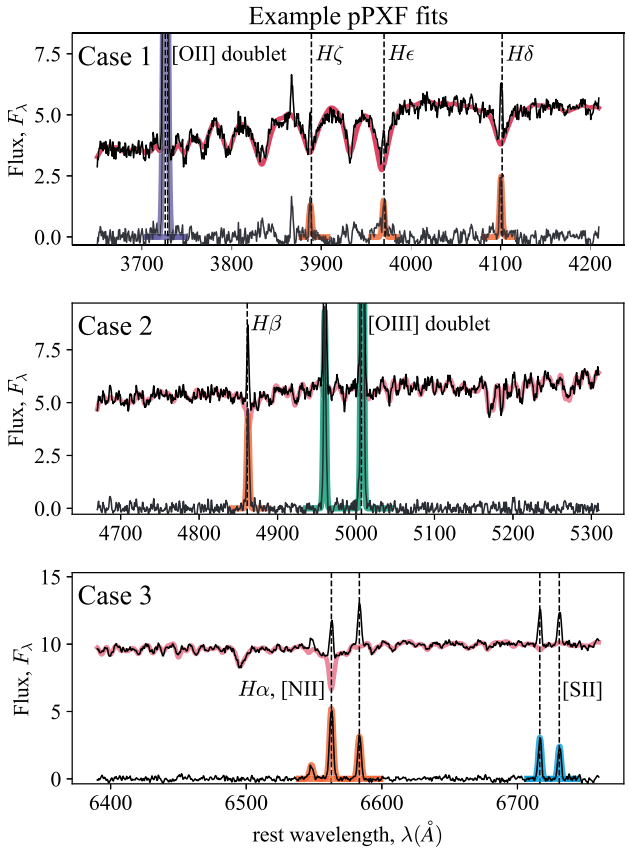

Figure 4. Example PPXF fits to each of the three spectral sections used to determine velocity curves. Each velocity curve consists of three components: stellar (red), hydrogen (orange), and forbidden (purple, green, and blue).

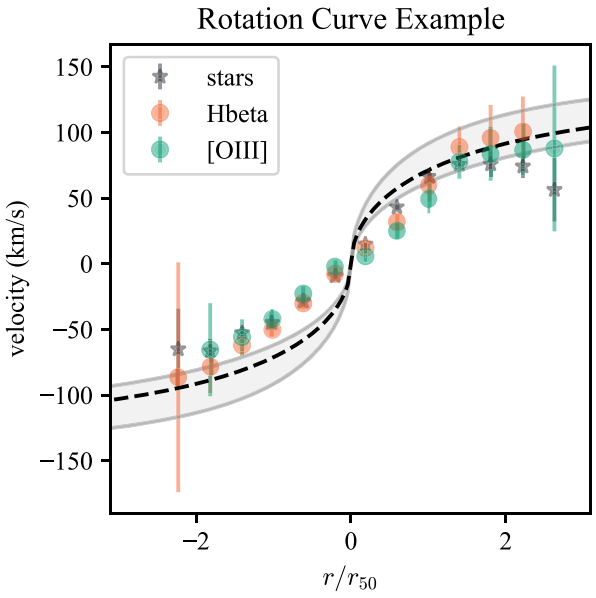

Figure 5. The object J170639.14+334103.4 was chosen randomly from our sample to provide an example of an orderly rotation curve, with a co-rotating disc of gas and stars. The stellar (grey stars), H β (orange circles), and [O III] (teal circles) velocities are shown as a function of normalized radius, where r_{50} is the r-band Petrosian 50 per cent radius. The dotted black line indicates the expected velocity curve for an NFW profile with concentration parameter $c = 10$. The shaded grey region represents the NFW curve expected from haloes with concentration parameter $c = 8$–15.

Section 3.3. To convert line-of-sight velocity measured in PPXF into rotational velocity, we correct for the disc inclination angle (see Appendix A). Zero velocity is measured at the Galaxy's kinematic centre, which is determined by the point of symmetry in the stellar velocity curve.

Fig. 5 shows the resulting rotational velocity curve for J170639.14+334103.4 as an example. Stellar velocity measurements are plotted as grey stars and the ionized gas velocities for H β and [O III] are shown as orange and teal circles, respectively. r_{50} refers to the 50 per cent SDSS r-band Petrosian radius. The grey shaded region shows the analytic prediction of the rotation curve assuming that the dark matter halo follows an NFW density profile (see Section 4.1).

4 RESULTS

We obtained circular velocity curves for the stellar and ionized gas components of all 50 Galaxies. Five Galaxies are excluded from the rest of this analysis based on the limited spatial extent of their stellar velocity curves. For three Galaxies (J024656.39–003304.8, J131503.77+223522.7, and J232028.21+150420.9), the spatial extent of their velocity curves was comparable (within 0.3 arcsec) with the seeing. NGC 1569 was excluded because the slit only covered the central 0.25 kpc of the Galaxy. J122342.82+581446.2 was excluded because we were unable to achieve a sufficient S/N ratio to obtain more than two stellar velocity measurements. Rotation curves for the remaining 45 Galaxies (26 AGNs and 19 star forming) included in this analysis are shown in Appendix B.

4.1 Comparison with NFW

The ΛCDM model predicts that dark matter haloes will follow an NFW profile, where the density steepens quickly in the inner regions and more slowly in the outer regions, forming a 'cusp' profile. However, observed dwarf galaxy rotation curves show a variety of slopes in their velocity profiles, some of which rise linearly with radius (Oman et al. 2015), implying underdense dark matter, or 'cores', in some galactic centres. This diversity in inferred dark matter profiles has been reported in a large number of observational studies and is yet to be explained by baryonic feedback models (e.g. Santos-Santos et al. 2020). Since both AGN and stellar feedback have been shown to move large quantities of gas, and thus would be capable of altering the dark matter distribution of their host galaxies (e.g. Governato et al. 2010; Martizzi, Teyssier & Moore 2013), the process of forming cores might be a complex interplay between multiple feedback modes. Any observed association between velocity curve shapes and AGN activity could help disentangle the role of AGN in shaping dwarf galaxy dark matter haloes.

To aid in visual identification of cores in our sample, we plot the NFW velocity curve of a ΛCDM halo corresponding to the predicted halo mass of each Galaxy as grey shaded regions in Figs 5 and 6, and all other velocity curve plots in Appendix B.

It is difficult to observationally constrain the halo mass of a galaxy, so one popular approach is to use abundance matching (e.g. Moster, Naab & White 2013). Abundance matching assumes a monotonic relation between stellar and halo masses and matches the cumulative abundance of galaxies on that relation. We used abundance matching to estimate the halo mass corresponding to each galaxy's stellar mass reported in the MPA-JHU catalogue (Kauffmann et al. 2003; Brinchmann et al. 2004; Tremonti et al. 2004). The only observational input is the stellar mass $M_\star$, so the halo mass M_h can be estimated using

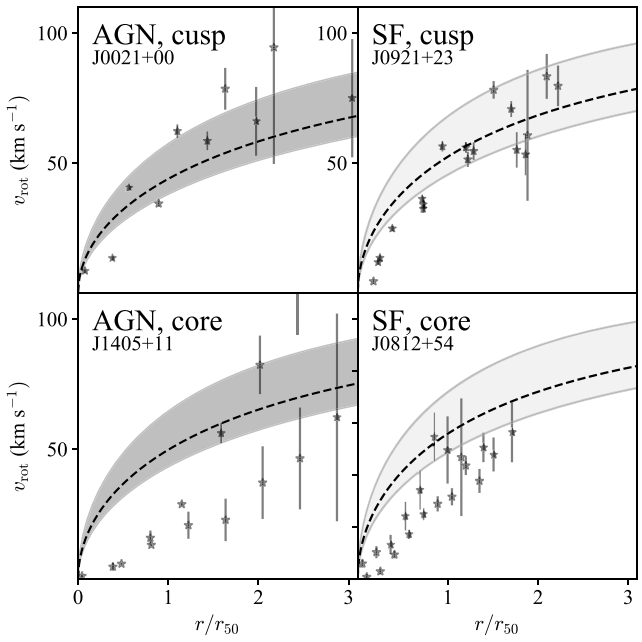

Figure 6. Four stellar absolute circular velocity curves are shown to demonstrate the variety of inner slopes found in our sample. Two examples of AGN are displayed in the left-hand panels and two star-forming Galaxies are shown on the right. Dashed black lines and shaded grey regions represent NFW velocity curves corresponding to a halo mass determined by abundance matching, with the MPA-JHU stellar mass as input. Stellar velocity curves showing agreement with the expected NFW profile are shown on the top two panels. The velocity profiles in the bottom panels rise slowly, indicating cored dark matter density profiles.

abundance matching (Moster et al. 2013, equation 2) as follows:

$$M_* = M_{\rm h}\left[2N\left(\frac{M_*}{M_1}\right)^{-\beta} + \left(\frac{M_{\rm h}}{M_1}\right)^{\gamma}\right]^{-1} \quad (1)$$

with four free parameters: N, the normalization parameter, a characteristic mass M_1, and low and high mass slopes β and γ, respectively.

From these estimated halo masses, we estimate a virial radius

$$r_{\rm v} = \left(\frac{3}{4}\frac{M_{\rm h}}{\pi\, v\, \rho_{\rm c}^0}\right)^{1/3}, \quad (2)$$

where $v = 200\,{\rm km\,s^{-1}}$ and $\rho_{\rm c}^0 = 277.5\,{\rm M_\odot\,kpc^{-1}}$. Assuming an NFW dark matter density profile, we construct a radial mass distribution (Łokas & Mamon 2001, equation 8):

$$M(r) = g(c)\left[\ln(1+cs) - \frac{cs}{1+cs}\right]M_{\rm h}, \quad (3)$$

where c is the concentration parameter, $s = r/r_v$, and $g(c) = [\ln(1+c) - c/(1+c)]^{-1}$. We estimate the circular velocity curve from the radial mass distribution using $v(r) = \sqrt{GM(r)/r}$. The dotted black line in Fig. 5 represents the rotation curve expected with an NFW profile with concentration parameter $c = 10$, and the shaded grey region was calculated assuming a concentration parameter between $c = 8$ and 15.

There is no clear correlation between rotational velocity slopes and AGN activity in our sample. Fig. 6 shows examples of two AGNs and two star-forming stellar absolute velocity curves in varying levels of agreement with their predicted NFW profiles. The lack of any association between current AGN activity and central mass deficits could be attributed to a difference in time-scales for AGN activity and core formation, or a number of other proposed factors not related to AGN (e.g. de Blok 2010). A solution to the cusp–core dilemma appears to be beyond the scope of this work, and it remains to be seen whether AGNs play a role in carving out cores in dwarf galaxies.

4.2 Peculiar gas

The gas in these dwarfs shows several distinct indications of non-rotational motion, which could be interpreted as inflows, outflows, or recently accreted gas. To identify disturbed gas kinematics, we designed a metric to quantify the relative offset between the gas and stellar rotation curves. $\Delta_{\rm off}$ is the weighted average of the absolute velocity offset between the stellar and gas component, divided by the average absolute stellar velocity.

$$\Delta_{\rm off} = \frac{|\bar{\Delta}_v|}{|\bar{v}_*|}, \quad (4)$$

where the weighted average of the absolute velocity offset is

$$|\bar{\Delta}_v| = \frac{\sum_i |v_{*,i} - v_{{\rm gas},i}|\, w_i}{\sum_i w_i} \quad (5)$$

and the weights are the inverse of the combined errors of each velocity measurement, $w_i = (\Delta v_{*,i}^2 + \Delta v_{{\rm gas},i}^2)^{-\frac{1}{2}}$.

This calculation considers the offset between the stellar and forbidden gas components because the [O II], [O III], and [S II] doublets are less affected by the subtraction of the stellar continuum and absorption than Balmer lines. Faint broad lines associated with the AGN may also contribute to the line profiles, adding further uncertainty in velocities measured using Balmer emission lines. The forbidden [O II], [O III], and [S II] doublets are not affected by such absorption or broad-line region features and therefore give more accurate velocity measurements.

Histograms of $\Delta_{\rm off}$ are shown in Fig. 7 and individual $\Delta_{\rm off}$ values are reported in the figures for each Galaxy in Appendix B. The top panel shows $\Delta_{\rm off}$ for all 45 Galaxies with rotation curves, the middle panel shows the distribution for all isolated Galaxies, and the bottom shows the distribution for all Galaxies that have at least one neighbour of comparable (or greater) mass (see Section 4.4 for a discussion on Galaxy environment). The histograms show a bimodal distribution, which is most pronounced in the middle panel. Based on this bimodality, we classify a Galaxy as 'disturbed' when $\Delta_{\rm off} \geq 0.75$ (dotted grey line).

Two Galaxies (J010005.94−011059.0 and J090613.75+561015.5) have $\Delta_{\rm off} < 0.75$ between the stars and forbidden emission lines, but the Balmer and forbidden gas components are offset from one another. Following the same approach, we determine the threshold for offset Balmer and forbidden emission components to be (H β – [O III] $\Delta_{\rm off} > 0.5$). Distinct kinematics associated with higher ionization emission lines is known as line stratification (see Section 4.2.1), and we count Galaxies with stratified emission lines among the Galaxies with disturbed gas. By this criterion, 25 of the 45 galaxies with rotation curves are disturbed. All rotation curves are plotted in Appendix B. The rotation curves showing orderly, co-rotating discs are shown in Fig. B1 and 25 disturbed rotation curves are shown in Fig. B2.

Of the 25 Galaxies with disturbed gas, 19 host AGN and 6 do not. The majority (73 per cent) of the AGNs in our sample have disturbed gas, while only 32 per cent of star-forming Galaxies have $\Delta_{\rm off} > 0.75$. We noticed distinct properties in the non-rotational motion exhibited in the disturbed gas, and we show examples of rotation curves exhibiting different types of disturbances. We observe gas that is generally offset from the stellar component, stratified emission

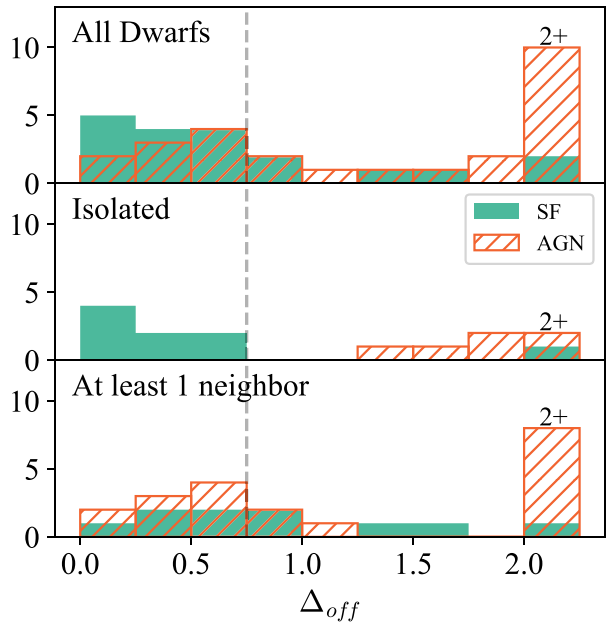

Figure 7. We define $\Delta_{\rm off}$ to be the weighted absolute average of the velocity offset between stars and gas, divided by the average absolute stellar velocity. This metric is used to quantify the degree of separation between the stellar and forbidden gas components. Based on the bimodal distribution of $\Delta_{\rm off}$ in our sample, we consider Galaxies with $\Delta_{\rm off} \geq 0.75$ to have kinematically disturbed gas.

lines, and counter-rotating gas. Examples of each type of disturbance are shown in Fig. 8.

4.2.1 *Line stratification*

In the stratified model of the narrow-line region (NLR), lower ionization gas resides on the outer parts of the NLR while higher ionization lines are generated closer to the AGN (e.g. Croom et al. 2002; Andika, Arifyanto & Kollatschny 2020). Distinct kinematics associated with emission lines of different ionization potentials imply a complex NLR that is stratified in ionization and wind speed. We observe stratified gas components in seven AGNs in our sample, with higher ionization lines showing higher velocities than lower ionization lines. This implies a decelerating outflow: where a high-velocity, high-ionization wind is generated near the AGN, and while the low-ionization gas in the outer region of the NLR flows more slowly.

We observe no correlation between wind speed and AGN luminosity, though the line stratification we observe in these seven Galaxies preferentially occurs in Galaxies that have outflows indicated by broad [O III] components. Plots of the stratified gas kinematics in these seven Galaxies can be found in Fig. B3.

4.2.2 *Counter-rotating*

Of the 45 Galaxies with rotation curves, 5 have counter-rotating gas and stellar components, as shown in Fig. 9. Counter-rotating gas and stars have long been explained as the effect of the accretion of gas clouds or small satellites after the formation of the stellar disc (e.g. Thakar & Ryden 1996; Thomas et al. 2006; Katkov, Sil'chenko & Afanasiev 2014). As mentioned in the introduction, S19 found that counter-rotating gas in dwarf galaxies requires substantial gas removal, either via black hole feedback or environmental effects from fly-by interactions with more massive systems. Interestingly, all five counter-rotating dwarfs in our sample host AGNs.

S19 also make several predictions about the present-day properties of counter-rotating dwarfs. In cases where re-accretion of gas is gradual, they find that counter-rotation can be very long lived (up to ∼2 Gyr). As a result, S19 predict no significant correlation with environment. Three counter-rotating Galaxies are isolated (J004214.99−104415.0, J080228.83+203050.2, and J093251.11+314145.0) and two (J094941.20+321315.9 and J130434.92+075505.0) have at least one neighbour with comparable mass.

An event that removes most of the original gas reservoir would quench star formation, making it likely that counter-rotating dwarfs will have older stellar populations and appear redder in colour. All five counter-rotating Galaxies discussed here have colours $u - r > 2$, which is redder than the average for our sample ($u - r = 1.83$). S19 also find a 30 per cent gas deficit in counter-rotating dwarfs at

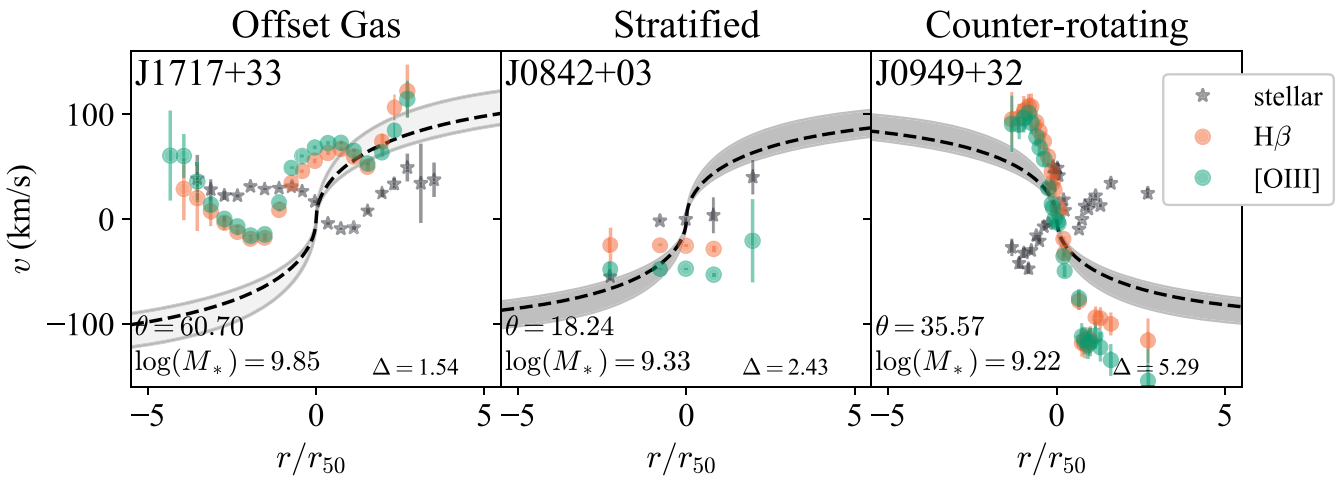

Figure 8. Examples of rotation curves where the gas is disturbed in different ways. In some instances, gas is offset from the stars without showing any clear sign of rotation (left). Some AGNs have stratified narrow-line components, where the Balmer and forbidden lines are kinematically distinct from one another (centre). Five Galaxies in our sample have gas and stellar discs rotating separately, and sometimes in opposite directions (right).

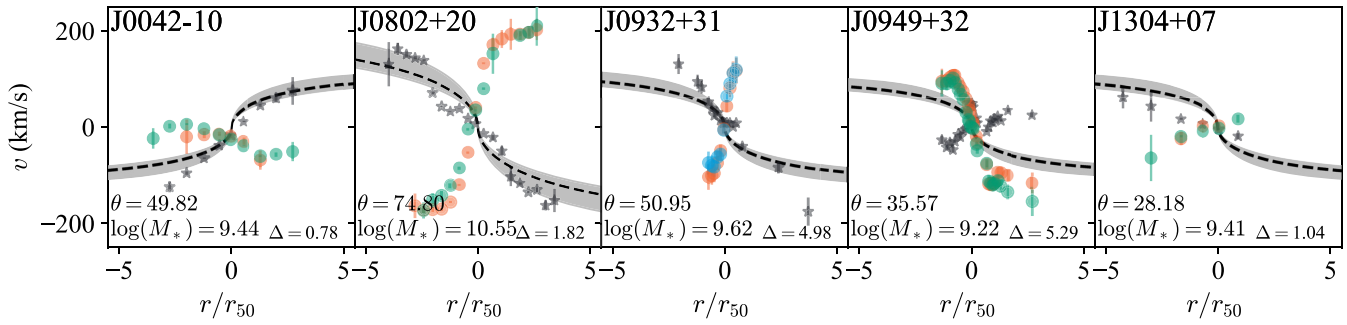

Figure 9. The rotation curves for five galaxies with counter-rotating gas are shown here. The colours are as in Fig. 8, and the blue dots in the middle panel indicate gas velocities measured from the [S II] doublet.

$z = 0$, relative to control galaxies at a fixed stellar mass. Though most of the Galaxies in our sample lack gas mass estimates, we can turn our attention to the six Galaxies with H I masses measured in the ALFALFA survey (Bradford et al. 2018). Of these six, five are not disturbed and one is counter-rotating (J094941.20+321315.9). The five co-rotating Galaxies with H I measurements have a wide range of gas fractions ($\frac{M_{\rm H\,I}}{M_*} \sim 0.23$–$7.3$), and the one counter-rotating has the smallest gas fraction ($\frac{M_{\rm H\,I}}{M_*} * = 0.16$). The gas component of J094941.20+321315.9 reaches velocities that exceed the predicted NFW curve, suggesting that this Galaxy inhabits a more massive halo than that predicted from its stellar mass.

4.3 Star formation suppression

While abundance matching enables us to infer halo masses based on stellar masses, maximum line-of-sight velocity measurements can be used to place lower limits on the true halo mass of each galaxy. If the measured lower limit of the halo mass of a galaxy exceeds the halo mass inferred from abundance matching to stellar mass, the galaxy can be said to have a lower star formation rate than that expected. Fig. 10 shows absolute line-of-sight velocity curves for the three Galaxies in our sample where this is most apparent. As in the previous figures, black dotted lines indicate the NFW curve predicted based on each Galaxy's stellar mass. Green curves mark the NFW curves associated with stellar masses $\log(M_\star/\,{\rm M}_\odot) = 10.5$, 11, and 12 and concentration parameter $c = 10$. The absolute line-of-sight velocity curves for the stellar (left), hydrogen Balmer emission (middle), and forbidden emission (right) components are shown. Line-of-sight velocities are plotted here in place of circular velocities to avoid errors introduced when correcting for disc inclination (Appendix A).

The three Galaxies shown in Fig. 10 were selected from our sample using a similar approach to the one used to identify disturbed gas in Section 4.2. We calculated the offset between each kinematic component ($v_{\rm los}$) and the predicted NFW curve $v_{\rm NFW}$:

$$\Delta_{v_{\rm los},\,\rm NFW} = \frac{\Sigma_i (v_{{\rm los},i} - v_{\rm NFW}) w_{{\rm los},i}}{\Sigma_i w_{{\rm los},i}}. \quad (6)$$

The distribution of $\Delta_{v_{\rm los},\,\rm NFW}$ values for each component revealed three outlying Galaxies that consistently fell above the threshold $\Delta_{v_{\rm los},\,\rm NFW} > 0.5$: J093251.11+314145.0, J094941.20+321315.9, and J140116.03+542507.4.

These Galaxies have measured velocity curves that far exceed the expected NFW profile, indicating that they inhabit much larger haloes than expected based on their stellar masses. Their small stellar masses and red colours ($u - r \geq 2.23$) suggest ongoing or recent star formation suppression. It is interesting to note that all three Galaxies host AGNs, and two have counter-rotating gas, consistent with the scenario where AGNs clear a substantial amount of gas from their hosts, limiting star formation.

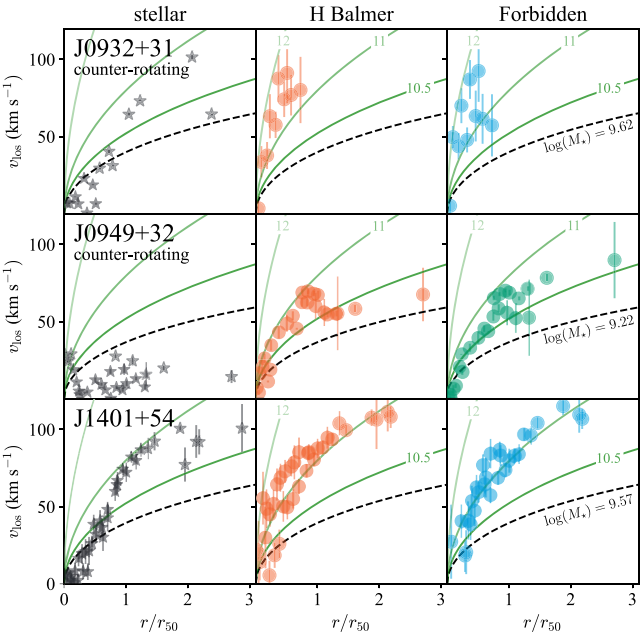

Figure 10. Absolute line-of-sight velocity ($v_{\rm los}$) measurements that far exceed the expected NFW velocity curves based on their stellar masses indicate overmassive dark matter haloes relative to the measured stellar mass, implying ongoing star formation suppression. Stellar (left), Balmer emission (centre), and forbidden emission (right) components are shown for the three Galaxies in our sample where this is most apparent. Green curves mark expected NFW velocity curves for Galaxies with stellar masses of $\log(M_\star) =$ 10.5, 11, and 12 and concentration parameter $c = 10$. Black dotted lines denote the expected NFW velocity curves based on each Galaxy's MPA-JHU stellar mass. All three of these Galaxies host AGNs, and two have counter-rotating gas components, which lends additional evidence potentially associating AGN with gas depletion and star formation suppression in dwarf galaxies.

4.4 Environment

To distinguish between the effects of environmental and secular processes on gas kinematics, we searched for luminous galaxies in the regions surrounding each dwarf. Following the method and criteria employed by Janz et al. (2017), we queried the SDSS DR12

and 2MASS Redshift survey catalogues for luminous neighbours with $M_{K_S} < -21.5$ mag and SDSS $r < -16$ mag. The completeness limit of this search is $M_{K_S} = -21.5$ mag at $z = 0.02$, corresponding to $M_* \sim 8 \times 10^9\,M_\odot$ (Geha et al. 2012). This limit is well below the magnitudes expected for galaxies in the mass range explored in this work, so extending the search to the redshift limit of our sample ($z = 0.05$) has no effect on completeness. The 2MASS Redshift Survey search revealed matches overlooked in the SDSS search due to missing redshifts, but SDSS optical counterparts existed for all 2MASS matches. We use SDSS DR12 *g*- and *r*-band photometry and the mass–magnitude relation of Bernardi et al. (2010) to estimate the masses of neighbouring galaxies.

We identify galaxies within 1.5 Mpc and $\pm 1000\,\mathrm{km\,s^{-1}}$ of each dwarf in this sample as neighbours. Using the *g*- and *r*-band mass–magnitude relation, we estimate the mass of each neighbour. In order to identify isolated galaxies, we count the number of neighbours with comparable mass (i.e. stellar mass $M_{\star,\mathrm{neighbour}} \geq 0.75 \times M_{\odot,\mathrm{dwarf}}$) within 1.5 Mpc and $\pm 1000\,\mathrm{km\,s^{-1}}$. The number of neighbours for each dwarf can be found in Table 2.

A recent study of 62 258 dwarf ($M_\star < 5 \times 10^9\,M_\odot$) galaxies finds no discernible difference between the environments of AGN and non-AGN dwarf galaxies, suggesting that environmental factors may not play a dominant role in triggering AGN (Kristensen, Pimbblet & Penny 2020). Similarly, we find no statistically significant link between the presence of AGN and environment. However, Kristensen et al. (2020) suggest that remnants of past interactions may be reflected in gas kinematics.

The importance of environment in disturbing gas kinematics can be explored by considering the bottom panel of Fig. 7, which shows the distribution of Δ_{off} for Galaxies with at least one neighbour of comparable (or greater) mass within 1.5 Mpc. Star-forming and AGN-hosting Galaxies with neighbours show varying degrees of gas disturbance, further supporting the notion that environment may not play a dominant role in triggering AGN activity. The most extreme values of Δ_{off} are associated with AGNs, suggesting that AGNs are capable of generating large-scale disturbances in their host galaxies' ISM, though the presence of AGN-hosting galaxies with undisturbed gas implies that this is not always the case.

On the other hand, isolated Galaxies show a distinct bimodal distribution, where star-forming Galaxies tend to have orderly rotating discs, and disturbed gas is almost always associated with AGN. Table 3 lists the seven disturbed, isolated Galaxies, six of which host AGNs. Two of these six isolated AGNs have counter-rotating gas, and three have outflows indicated by distinct broadened components in [O III]λ5007, as in Paper I. To clarify, the outflows in these four Galaxies are identified with multicomponent Gaussian fits to the [O III] line profile; disturbed gas is determined here by a velocity offset between the narrow component of the emission lines from the stellar component.

The single isolated and disturbed star-forming Galaxy, J101440.21+192448.9, was originally included in our sample based on broad lines in Hα (Reines et al. 2013), which later faded, likely due to transient stellar activity (Baldassare et al. 2016). This object is classified as an outflow Galaxy in Paper I based on broadened wings in its [O III] emission line profile. Follow-up Integral Field Unit (IFU) observations with KCWI revealed that the rotation axis of J101440.21+192448.9 is in fact parallel to the slit position in our LRIS observations (Liu et al., in preparation). Since the slit is not aligned with the stellar disc, these velocity measurements do not reflect the true rotational velocity of this Galaxy.

Follow-up KCWI observations were obtained for eight objects in this sample (Liu et al., in preparation). These IFU observations produce line-of-sight velocities that agree with our long-slit measurements and confirm that in all other cases, the LRIS slit was oriented perpendicular to the rotational axes, as intended. Proper slit orientation for the remainder of the sample should be verified with similar follow-up IFU observations, though the confirmation of correct slit placement in all but one Galaxy is encouraging. Since J101440.21+192448.9 is an active star-forming Galaxy with supernova-driven outflows, it is reasonable to surmise that bright star-forming regions could outshine the rest of the disc, confusing the photometric fit used to determine slit placement. This calls into question the slit placement for other Galaxies with non-rotational kinematics and signs of active star formation, such as J171759.66+332003.8.

5 SUMMARY

From Keck LRIS long-slit spectroscopy, we measured rotational velocity curves of 45 dwarf Galaxies. Our sample consists of 26 Galaxies with AGNs and a control sample of 19 star-forming Galaxies with no optical or IR evidence of AGNs. The rotation curves are decomposed into stellar, Balmer emission, and forbidden emission components. In order to investigate the potential effects of AGN on gas kinematics in this sample, we quantified velocity offsets between stellar and gas components. We summarize our conclusions below.

(i) We detect counter-rotating gas in 5 of 45 Galaxies, and AGNs are present in all 5 cases. A study of the occurrence, properties, and evolutionary history of counter-rotating Galaxies in Illustris (S19) finds that removal and re-accretion of gas is necessary for counter-rotating gas discs to form, and that periods of AGN activity are sometimes associated with large drops in gas mass. We find that the properties of the counter-rotating dwarfs in our sample agree with present-day properties of counter-rotating dwarf galaxies predicted from Illustris.

(ii) We use the weighted average of velocity offsets between stellar spectra and emission lines to identify disturbed gas kinematics. We find disturbed gas in 25 out of 45 Galaxies in our sample. Of the 26 AGNs in our sample, 19 (or 73 per cent) have disturbed gas. Star-forming Galaxies tend to have orderly, co-rotating gas discs, with only 32 per cent showing disturbed gas.

(iii) At least three Galaxies in our sample have line-of-sight velocities far exceeding those expected based on their stellar masses. These line-of-sight velocities constitute a lower limit estimate of true halo mass, indicating that these Galaxies inhabit much more massive dark matter haloes than expected based on their small stellar masses. This potential evidence of ongoing star formation suppression is most apparent in three AGN-hosting Galaxies within our sample, two of which have counter-rotating gas. This suggests that AGNs could be associated with gas removal and star formation suppression in dwarf galaxies. A detailed study of the star formation histories of these Galaxies is warranted.

(iv) In the absence of environmental influence, kinematically disturbed gas is expected to be caused by secular processes. 15 dwarfs in our sample are isolated, with no neighbouring galaxies of comparable mass within 1.5 Mpc and $\pm 1000\,\mathrm{km\,s^{-1}}$. Of these, seven Galaxies have disturbed gas. We find that six out of seven isolated Galaxies with disturbed gas host AGNs.

Our findings imply that AGNs play an important, and perhaps dominant, role in disturbing gas and limiting star formation in dwarf galaxies. This represents additional evidence of the importance of AGN-driven winds in dwarf galaxy evolution and further highlights the importance of including AGN feedback in galaxy formation models. A detailed follow-up IFU study of ionized gas kinematics in a subset of these Galaxies is in progress (Liu et. al., in preparation).

Table 2. (1) [a]indicates objects excluded from this study. (2) Redshift is calculated by fits to stellar absorption lines in LRIS spectra using PPXF. (3) Stellar mass reported in the MPA-JHU catalogue. (4) [b] Black hole mass lower limits derived using Eddington Luminosity arguments (M14). [c] Black hole mass estimated using $M_{\rm BH} \propto R\Delta V^2/G$, where ΔV is measured from broad H α; extrapolating the BLR radius–luminosity relation extends into the low-mass regime (R13). (5) SDSS Petrosian radius containing 50 per cent of *r*-band flux, in kiloparsec. (6) Classification of dominant ionization source based on Gaussian fits to emission lines using the process described in Section 3.2. The spectra were extracted from the central 1 kpc of each Galaxy. (7) Same as (6) but for He II classification (S15). (8) The number of galaxies with comparable mass within 1.5 Mpc. (9) Classified as disturbed (see Section 4.2). (10) Gas is clearly rotating and offset from stellar component. (11) Has an outflow identified by an additional broad component as defined in Paper I. (12) Narrow emission lines are stratified (see Section 4.2.1).

Abbreviated name (1)	Redshift (2)	log (M_*) (3)	log ($M_{\rm BH}$) (4)	r_{50} (kpc) (5)	BPT (6)	He II (7)	Neighbours (8)	Disturbed (9)	Counter-rotating (10)	Outflow (11)	Stratified (12)
J0021+00	0.0180	9.15	–	0.89	AGN	AGN	7	–	–	–	–
J0042−10	0.0359	9.44	–	1.34	AGN	AGN	5	✓	✓	–	–
J0100−01	0.0515	9.44	–	0.99	Comp.	Comp.	5	✓	–	✓	–
J0156−00	0.0450	9.39	–	1.91	SF	SF	13	✓	–	–	–
J0246−00[a]	0.0464	9.35	5.7[c]	1.34	AGN	AGN	37	–	–	–	–
J0300+00	0.0095	8.72	–	2.11	SF	SF	0	–	–	–	–
NGC 1569[a]	$-80\,{\rm km\,s^{-1}}$	8.56	–	7.09	SF	SF	–	–	–	✓	–
J0755+24	0.0290	8.85	–	1.78	SF	SF	3	–	–	–	–
J0802+10	0.0145	9.60	3.6[b]	1.29	AGN	AGN	3	–	–	–	–
J0802+20	0.0286	10.6	–	1.97	Comp.	AGN	0	✓	✓	–	–
J0811+23	0.0157	9.06	4.4[c]	0.58	AGN	AGN	2	✓	–	✓	✓
J0812+54	0.0086	9.29	–	1.49	SF	SF	0	–	–	–	–
J0840+18	0.0149	9.13	4.3[c]	0.94	AGN	AGN	2	✓	–	✓	–
J0842+03	0.0289	9.33	–	0.75	Comp.	AGN	2	✓	–	✓	✓
J0851+39	0.0407	9.28	5.4[c]	1.70	AGN	AGN	2	–	–	–	–
J0906+56	0.0465	9.37	5.4[c]	1.51	AGN	AGN	5	✓	–	✓	–
J0911+61	0.0263	8.95	–	2.03	SF	SF	7	✓	–	–	–
J0921+23	0.0281	9.27	–	1.27	SF	SF	0	–	–	–	–
J0932+31	0.0153	9.62	3.5[b]	0.58	AGN	AGN	0	✓	✓	–	–
J0948+09	0.0103	8.73	4.2[b]	0.73	Comp.	AGN	5	✓	–	–	✓
J0949+32	0.0051	9.22	4.1[b]	0.58	Comp.	AGN	6	✓	✓	–	–
J0954+47	0.0326	9.47	4.9[c]	1.75	AGN	AGN	0	✓	–	✓	–
J1002+59	0.0093	9.60	4.1[b]	1.12	AGN	Comp.	1	✓	–	–	✓
J1005+12	0.0093	9.64	4.8[b]	0.97	AGN	AGN	0	✓	–	✓	–
J1009+26	0.0143	8.75	5.1[c]	0.62	AGN	AGN	0	✓	–	✓	–
J1014+19	0.0284	8.56	–	0.88	SF	SF	0	✓	–	✓	–
J1143+55	0.0269	8.92	–	1.03	SF	SF	1	–	–	–	–
J1223+58[a]	0.0146	9.39	6.1[b]	1.01	AGN	AGN	6	–	–	–	–
J1304+07	0.0479	9.41	–	1.13	AGN	AGN	16	✓	✓	–	–
J1307+52	0.0259	9.10	–	1.18	SF	SF	2	–	–	–	–
J1315+22[a]	0.0226	9.20	–	1.58	SF	SF	1	–	–	–	–
J1343+25	0.0280	9.19	–	3.09	SF	SF	3	–	–	–	–
J1401+54	0.0059	9.57	3.2[b]	0.59	AGN	AGN	5	–	–	–	–
J1402+09	0.0195	8.83	–	0.79	AGN	AGN	26	✓	–	–	–
J1405+11	0.0178	9.23	–	1.15	AGN	AGN	4	–	–	–	–
J1407+50	0.0070	8.72	–	0.77	Comp.	AGN	8	–	–	–	–
J1412+10	0.0324	8.99	–	0.56	AGN	AGN	3	✓	–	–	–
J1442+20	0.0426	8.89	–	0.89	AGN	AGN	1	✓	–	✓	✓
J1458+11	0.0198	9.91	–	2.40	SF	SF	0	–	–	–	–
J1511+23	0.0143	9.68	–	1.01	SF	SF	0	–	–	–	–
J1546+03	0.0132	9.49	–	2.05	SF	AGN	3	–	–	–	–
J1608+12	0.0166	9.75	–	2.65	SF	SF	0	–	–	–	–
J1623+39	0.0172	9.22	–	2.68	SF	SF	2	✓	–	–	–
J1623+45	0.0064	9.41	–	0.82	AGN	AGN	0	✓	–	–	–
J1644+43	0.0178	9.53	–	0.86	SF	SF	0	–	–	–	–
J1706+33	0.0301	9.41	–	1.95	SF	SF	7	–	–	–	–
J1717+33	0.0151	9.85	–	1.03	SF	SF	1	✓	–	✓	–
J1721+28	0.0280	10.0	–	3.49	SF	SF	0	–	–	–	–
J1722+28	0.0281	9.23	–	1.71	SF	SF	3	✓	–	–	–
J2320+15[a]	0.0130	9.57	3.7[b]	0.59	AGN	AGN	6	–	–	–	–

Table 3. Seven Galaxies in our sample have disturbed gas kinematics and no neighbours of comparable mass within 1.5 Mpc and ±1000 km s^{-1}. Six of them host AGNs, two have counter-rotating gas, and four have outflows indicated by broad wings in their [O III]5007 emission line profiles. $u - r$ colour is based on SDSS cModelMag photometry.

Name	log ($M_\star$)	AGN	Counter-rotating	Outflow (Paper I)	$u - r$ colour
J0802+20	10.6	✓	✓	–	2.39
J0932+31	9.6	✓	✓	–	2.23
J0954+47	9.5	✓	–	✓	2.20
J1005+12	9.6	✓	–	✓	2.16
J1009+26	8.7	✓	–	✓	1.91
J1014+19	8.6	–	–	✓	1.25
J1623+45	9.4	✓	–	–	2.13

Multiphase gas kinematic measurements, gas mass measurements, and comparison with simulations run with detailed AGN feedback models are necessary for a full understanding of AGN feedback in dwarf galaxies.

ACKNOWLEDGEMENTS

We would like to thank the anonymous referee, whose careful reading and thoughtful feedback has helped to improve and clarify this manuscript. Support for this program was provided by the National Science Foundation, under grant number AST 1817233. Additional support was provided by National Aeronautics and Space Administration (NASA) through a grant from the Space Telescope Science Institute (Programme AR-14582.001-A), which is operated by the Association of Universities for Research in Astronomy, Incorporated, under NASA contract NAS5-26555. The data presented herein were obtained at the W. M. Keck Observatory, which is operated as a scientific partnership among the California Institute of Technology, the University of California, and NASA. The observatory was made possible by the generous financial support of the W. M. Keck Foundation. The authors wish to recognize and acknowledge the very significant cultural role and reverence that the summit of Mauna Kea has always had within the Indigenous Hawaiian community. We are most fortunate to have the opportunity to conduct observations from this mountain. Some of the data presented herein were obtained using the University of California Irvine Remote Observing Facility, made possible by a generous gift from John and Ruth Ann Evans. This research has made use of the NASA/IPAC Extragalactic Database (NED), which is operated by the Jet Propulsion Laboratory, California Institute of Technology, under contract with NASA.

DATA AVAILABILITY

The data underlying this article will be shared on reasonable request to the corresponding author.

REFERENCES

Andika I. T., Arifyanto M. I., Kollatschny W., 2020, Astron. Nachr., 341, 300
Baldassare V. F. et al., 2016, ApJ, 829, 57
Baldassare V. F., Geha M., Greene J., 2020, ApJ, 896, 10
Baldwin J. A., Phillips M. M., Terlevich R., 1981, PASP, 93, 5
Bernardi M., Shankar F., Hyde J. B., Mei S., Marulli F., Sheth R. K., 2010, MNRAS, 404, 2087
Birchall K. L., Watson M. G., Aird J., 2020, MNRAS, 492, 2268
Blanton M. R. et al., 2017, AJ, 154, 28
Boylan-Kolchin M., Bullock J. S., Kaplinghat M., 2011, MNRAS, 415, L40
Bradford J. D., Geha M. C., Greene J. E., Reines A. E., Dickey C. M., 2018, ApJ, 861, 50
Bradley L. et al. , 2019, Astropy/photutils: v0.6. available at: https://doi.org/10.5281/zenodo.2533376
Brinchmann J., Charlot S., White S. D. M., Tremonti C., Kauffmann G., Heckman T., Brinkmann J., 2004, MNRAS, 351, 1151
Rockosi C. et al., 2010, in McLean I. S., Ramsay S. K., Takami H., eds, Proc. SPIE Conf. Ser. Vol. 7735, Ground-Based and Airborne Instrumentation for Astronomy III. SPIE, Bellingham, p. 77350R
Cann J. M., Satyapal S., Abel N. P., Blecha L., Mushotzky R. F., Reynolds C. S., Secrest N. J., 2019, ApJ, 870, L2
Cappellari M., 2017, MNRAS, 466, 798
Croom S. M. et al., 2002, MNRAS, 337, 275
de Blok W. J. G., 2010, Adv. Astron., 2010, 789293
Dickey C.M., Geha M., Wetzel A., El-Badry K., 2019, ApJ, 884, 180
Emerick A., Bryan G. L., Mac Low M.-M., 2018, ApJ, 865, L22
Flores R. A., Primack J. R., 1994, ApJ, 427, L1
Foreman-Mackey D., Hogg D. W., Lang D., Goodman J., 2013, PASP, 125, 306
Geha M., Blanton M. R., Yan R., Tinker J. L., 2012, ApJ, 757, 85
Genel S. et al., 2014, MNRAS, 445, 175
Giovanelli R., Haynes M. P., Salzer J. J., Wegner G., da Costa L. N., Freudling W., 1994, AJ, 107, 2036
Governato F. et al., 2010, Nature, 463, 203
Hu C.-Y., 2019, MNRAS, 483, 3363
Janz J., Penny S. J., Graham A. W., Forbes D. A., Davies R. L., 2017, MNRAS, 468, 2850
Jarrett T. H. et al., 2011, ApJ, 735, 112
Katkov I. Y., Sil'chenko O. K., Afanasiev V. L., 2014, MNRAS, 438, 2798
Katz H. et al., 2020, MNRAS, 494, 2200
Kauffmann G. et al., 2003, MNRAS, 346, 1055
Kaviraj S., Martin G., Silk J., 2019, MNRAS, 489, L12
Kewley L. J., Dopita M. A., Sutherland R. S., Heisler C. A., Trevena J., 2001, ApJ, 556, 121
Klypin A., Kravtsov A. V., Valenzuela O., Prada F., 1999, ApJ, 522, 82
Kristensen M. T., Pimbblet K., Penny S., 2020, MNRAS, 496, 2577
Lovell M. R., Frenk C. S., Eke V. R., Jenkins A., Gao L., Theuns T., 2014, MNRAS, 439, 300
Manzano-King C. M., Canalizo G., Sales L. V., 2019, ApJ, 884, 54
Martin C. L., 1998, ApJ, 506, 222
Martín-Navarro I., Mezcua M., 2018, ApJ, 855, L20
Łokas E. L., Mamon G. A., 2001, MNRAS, 321, 155
Martizzi D., Teyssier R., Moore B., 2013, MNRAS, 432, 1947
Moore B., Ghigna S., Governato F., Lake G., Quinn T., Stadel J., Tozzi P., 1999, ApJ, 524, L19
Moran E. C., Shahinyan K., Sugarman H. R., Vélez D. O., Eracleous M., 2014, AJ, 148, 136
Moster B. P., Naab T., White S. D. M., 2013, MNRAS, 428, 3121
Navarro J. F., Frenk C. F., White S. D. M., 1997, ApJ, 490, 493
Oh S.-H., Brook C., Governato F., Brinks E., Mayer L., de Blok W. J. G., Brooks A., Walter F., 2011, AJ, 142, 24
Oh S.-H. et al., 2015, AJ, 149, 180
Oke J. B. et al., 1995, PASP, 107, 375
Oman K. A. et al., 2015, MNRAS, 452, 3650
Penny S. J. et al., 2018, MNRAS, 476, 979
Read J. I., Wilkinson M. I., Evans N. W., Gilmore G., Kleyna J. T., 2006, MNRAS, 367, 387
Reines A. E., Greene J. E., Geha M., 2013, ApJ, 775, 116
Rocha M., Peter A. H. G., Bullock J. S., Kaplinghat M., Garrison-Kimmel S., Oñorbe J., Moustakas L. A., 2013, MNRAS, 430, 81
Santos-Santos I. M. E. et al., 2020, MNRAS, 495, 58
Sartori L. F., Schawinski K., Treister E., Trakhtenbrot B., Koss M., Shirazi M., Oh K., 2015, MNRAS, 454, 3722
Satyapal S., Abel N. P., Secrest N. J., 2018, ApJ, 858, 38
Shirazi M., Brinchmann J., 2012, MNRAS, 421, 1043
Simon J. D., Bolatto A. D., Leroy A., Blitz L., Gates E. L., 2005, ApJ, 621, 757